# $^{28}Si + ^{14}N$ orbiting interaction

B. Shivakumar
*A.W. Wright Nuclear Structure Laboratory, Yale University, New Haven, Connecticut 06511*
*and Physics Division, Oak Ridge National Laboratory, Oak Ridge, Tennessee 37831*

D. Shapira and P. H. Stelson
*Physics Division, Oak Ridge National Laboratory, Oak Ridge, Tennessee 37831*

S. Ayik
*Tennessee Technological University, Cookeville, Tennessee 38505*

B. A. Harmon*
*University of Virginia, Charlottesville, Virginia 22901*
*and Physics Division, Oak Ridge National Laboratory, Oak Ridge, Tennessee 37831*

K. Teh
*Physics Department, Vanderbilt University, Nashville, Tennessee 37235*

D. A. Bromley
*A.W. Wright Nuclear Structure Laboratory, Yale University, New Haven, Connecticut 06511*
(Received 13 August 1987)

The charge and mass distribution of orbiting yields from the $^{28}Si + ^{14}N$ interaction have been studied at center of mass energies between 30 and 56.7 MeV. The data indicate that the orbiting system lives sufficiently long for the exit channel yields to be determined by phase space considerations. The data are compared with compound nucleus and orbiting calculations, and clearly favor the latter. Further comparisons between the data and the orbiting calculations indicate that full phase space equilibration of the orbiting yields is hindered at low excitation energies by the inaccessibility of single nucleon transfer channels. Also evident in the data is a correlation in the behaviors of the charge width, mass width, and final product kinetic energies, which is interpretable as arising from a maximum angular momentum that the $^{28}Si + ^{14}N$ orbiting composite can sustain.

## I. INTRODUCTION

A rotating dinuclear molecular complex (DMC) is often formed in the early stages of an interaction between heavy ions. The existence of such a complex has been inferred through detection of significant yields of binary reaction products ($\approx 10\%$ to 20% of the fusion yield). These resemble the entrance channel, and have been measured at backward angles where such yields are not obscured by direct processes.[1-6] The observed yields of such products can be identified with those DMC's that fragment during the course of their first revolution, and the process of fusion can be identified with those DMC's that live for a larger number of revolutions.[6,7] It is our contention, then, that if $P_1$ is the probability of forming the DMC, and $P_2$ that of the decay of the DMC into orbiting products, then the probability of fusion is $P_3 = P_1(1-P_2)$. We have studied the $^{28}Si + ^{14}N$ orbiting interaction[6] to establish whether, in the presence of all other signatures of the orbiting process, we could establish that orbiting interactions lasted sufficiently long for the exit channel yields to be determined by phase space considerations. The $^{28}Si + ^{14}N$ system was chosen for this study because it was very similar in mass to the $^{28}Si + ^{12}C$ system, which we have investigated in great detail in previous measurements.[2,8] These two systems differed rather dramatically, however, in the availability at low excitation energies, of dinuclear channels into which the DMC can break. While the $^{28}Si + ^{12}C$ system has few such channels, the $^{28}Si + ^{14}N$ system has several. This greatly enhances the phase space accessible to particle exchange, even at low excitation energies, in the $^{28}Si + ^{14}N$ system. Energy and phase space considerations dictate that if the duration of orbiting in the $^{28}Si + ^{14}N$ interaction exceeds the time required for charge and mass equilibration via particle exchange, $^{12}C$ should be the most common product nucleus; otherwise, $^{14}N$ should be the most common one. The results of our measurement show that the $^{12}C/^{14}N$ yield ratio exceeds unity over the range of energies for which the measurement was made, demonstrating clearly that the $^{28}Si + ^{14}N$ orbiting complex indeed lives sufficiently long for the distribution of yields in the exit channel to reflect charge and mass equilibration. We present, herein, details of the experimental techniques and data analyses that were brought to bear in arriving at these results, followed by discussions of the observations and comparisons to model calculations.

In our experiments, which were performed at the Oak Ridge National Laboratory Holifield Heavy Ion Research Facility, $^{28}Si$ beams with energies between 100 and 170 MeV were used to bombard a $^{14}N$ supersonic gas jet target. Targetlike reaction products ($5 < Z < 10$)

 ©1988 The American Physical Society

were detected at laboratory angles between 3° and 11° at 140 MeV, between 3° and 7° at 130, 160, and 170 MeV, and at 5° at 100, 110, 120, and 150 MeV. In a kinematically reversed reaction ($^{14}N$ beam on a $^{28}Si$ target), this corresponds to measurements in the center of mass angular range from 175° to 155°.

## II. EXPERIMENTAL PROCEDURE: APPARATUS

A schematic diagram of the experimental apparatus is shown in Fig. 1. $^{28}Si$ beams from the accelerator were collimated by two circular slits $S_1$ and $S_2$ of diameter 0.73 mm spaced about 75 cm apart, with the nearest about 70 cm from the scattering chamber. The presence of these slits ensured that the beam did not strike the differential pumping slits $D_{1,2,3}$ but passed through them to strike the target. Reaction products were detected at the focal plane of an Enge split-pole magnetic spectrograph by a hybrid ionization chamber. Using the position, energy, and energy loss signals provided by this detector, it was possible to identify the reaction products both in terms of their mass and their charge. Beam profile diagnostics were provided by four quartz viewers $Q_{1,2,3,4}$. Additional diagnostic information was provided in the target region via beam current integration. In the experiment, the currents integrated on the electrically isolated aperture $D_1$ were minimized to about 3% of the current integrated on the body of the gas jet target, which served as the beam dump. Typical beam currents during the experiment were in the range 20–80 particle nA.

### A. The target

Figure 2 shows a schematic side view of the supersonic gas-jet target.[9] The apparatus consists of four differentially pumped volumes (denoted as I–IV) separated by slits of diameter $<3$ mm. During routine operation, with a pressure of 600 Torr at the inlet to the nozzle, the pressures in the four volumes were measured to be 1.38, 0.35, $3.9\times10^{-4}$, and $3.4\times10^{-6}$ Torr, respectively. The pressure in the beam line was always below $3\times10^{-8}$ Torr. The target gas—99% $N_2$ and 1% Xe—enters the interaction region through a Laval nozzle whose rectangular exit aperture measured 1.27

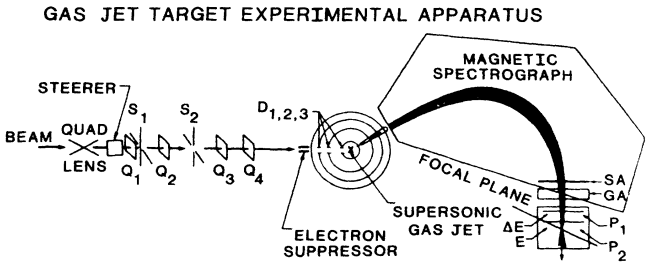


FIG. 1. The experimental arrangement used for the $^{28}Si+^{14}N$ experiment. $Q_{1,2,3,4}$ are quartz viewers. $S_1$ and $S_2$ are rotatable circular slits adjustable to 0.75, 1.75, 3, and 25 mm diameters. $D_{1,2,3}$ are differential pumping slits. $SA$ and are solid and gas absorbers, respectively. $P_1$ and $P_2$ are position sensing wires.

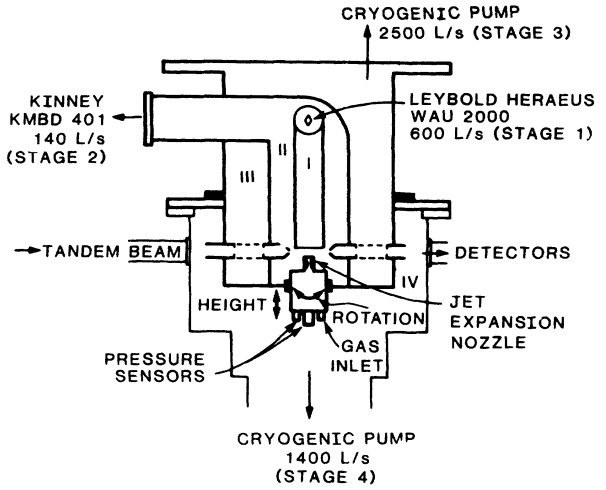


FIG. 2. A schematic side view of the supersonic gas jet target.

mm×2.54 mm. The target thickness was measured to be $3\times10^{17}$ atoms/cm$^2$. The Xe in the target was added to permit a normalization of the yields of products from orbiting interactions to the yields of elastically scattered particles from the Xe. Since the target material was being pumped away continuously, there was no carbon or other buildup. This is a ubiquitous problem with solid targets—targets which also impose limits, because of charge buildup and thermal damage, on the beam intensity that can be handled. The purity of the target was determined by the purity of the inlet gas, and this is crucial to experiments such as these, where continuum spectra are being measured.

The target thickness was maximized by positioning the gas jet nozzle such that the ion beam interacted with the first high density region downstream of the nozzle exit. In a well designed target this adjustment is crucial, and it provides a supersonic jet that is well focused. The small physical extent of the target then makes it possible to take advantage of the kinematic compensation provided by the Enge spectrograph. We therefore not only have a thicker target but also a larger detection solid angle. This adjustment was done optically, and we had to be careful to ensure that the apertures restricting the extent of the ion beam were positioned such that the ion beam could not strike the nozzle directly. Also a measurement had to be made to determine the relative orientation of the gas-jet apparatus exit aperture and the entrance aperture of the spectrograph (Fig. 2 in Ref. 9) as denoted by the scales showing their respective angular positions.

### B. The detection system

The reaction products were focused by an Enge split-pole spectrograph into a hybrid ionization chamber (HIC).[10] Figure 3 is a schematic side view of the HIC. Two position-sensing wires labeled $A$ (normal to the page) provide the information needed to determine particle trajectories. The total energy signal $E$ is obtained from the cathode, labeled $G$, which forms part of a Faraday cage with the metallic strips labeled $F$ which help

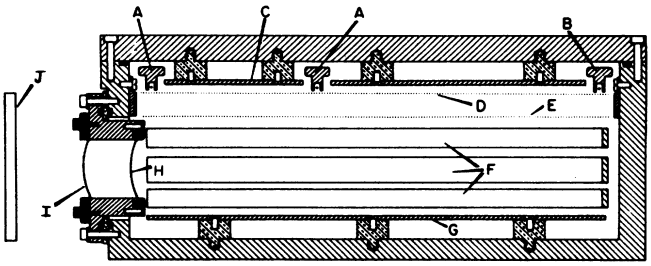


FIG. 3. Schematic side view of the hybrid ionization chamber (HIC) (Ref. 10). *A* denotes position sensitive proportional counters. *B* denotes reject proportional counter. *C* denotes $\Delta E$ electrode. *D* denotes ionization chamber Frisch grid. *E* denotes grid capacitively coupled to the cathode providing the energy signal. *F* denotes Cathode strips. *G* denotes Cathode. *H* denotes counter entrance window. *I* denotes gas absorber window. *J* denotes solid absorber.

maintain a uniform field gradient, and an aluminized Mylar window *H*, through which ions enter the detector. *D* is a grid. The region between *H* and a second window *I* forms a gas absorber. *J* is a solid absorber. The energy loss ($\Delta E$) information is obtained from the segmented anode *C*. *B* is a veto wire detecting particles that are not stopped within the counter. Using the *E*, $\Delta E$, and position information provided by the detector, the reaction products could be identified uniquely by atomic charge *Z*, mass number *A*, and energy.

The maximum usable solid angle of the detection system was 2.4 msr, and was limited by the exit aperture of the gas-jet assembly. Additional gas and solid absorbers could be introduced in front of the HIC to prevent the elastically scattered ions from entering the counter. This increased the data taking efficiency of the experiment, as will be discussed below. The detector was mounted at an angle of 45° to the focal plane of the spectrograph. Consequently, the trajectories of the particles entering the HIC were approximately normal to the entrance window of the counter and the absorbers. This is crucial in maintaining sufficient accuracy in the measurement of the total energy of the detected ions. Also, for the same purpose, it is necessary to ensure that the pressure within the HIC exceeds the pressure in the gas absorber so that the two windows *H* and *I* are bowed in the same direction.

### C. The charge state efficiency

The reaction products resulting from an interaction between a projectile and a target are emitted with a range of atomic charge states *q*. The actual charge state distribution is determined by the target thickness and the energy of the ion species. On passing into the spectrograph, depending on the atomic charge state, an ion with a given energy traces orbits of different radii. Since the HIC is 40 cm wide, only some of these orbits are detected. This creates an efficiency problem. Figure 4 is a plot of the energy versus the momentum of carbon, nitrogen, oxygen, and fluorine nuclei from the $^{28}Si+^{14}N$ interaction, detected in the HIC in a preliminary study. In all figures, the upper group of three lines corresponds to the charge state $q=Z$ and the lower group to $q=Z-1$. Within these groups, the individual lines correspond to the different isotopes of the same element. In the lower four panels it is clear that the yield is distributed over two charge states. Also, by examining the energy axes of these plots, it is obvious that the HIC is not wide enough to capture the whole dynamic range of both charge states. Hence, it is desirable to induce all

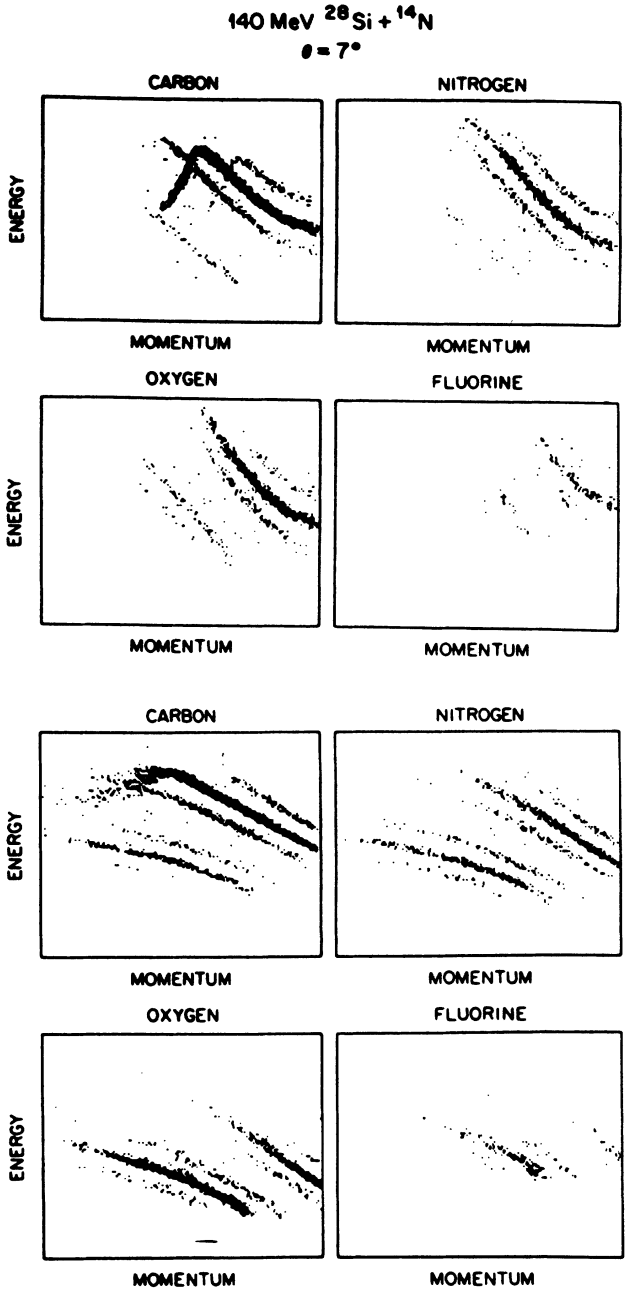


FIG. 4. A plot showing the effects of adding an Al Stripper foil at the entrance to the spectrograph. The lower four figures were taken without this foil, and the upper four figures with the foil. In each figure, the upper group of three lines corresponds to charge state $q=Z$, and the lower group to $q=Z-1$. Within each group, the individual lines correspond to different isotopes of the same element. The addition of the foil moves the yield from the lower charge state to the higher.

reaction products with the same $Z$ to have the same charge state $q$. This can be accomplished with a certain degree of success by placing a stripper foil at the entrance to the spectrograph. The upper four plots of Fig. 4 show the results of such a modification to the experimental arrangement using a 100 $\mu g/cm^2$ Al foil. It is evident that the bulk of the isotopic yields is now detected in their highest ($q=Z$) charge state. Such a procedure is needed only in situations where the target used is not thick enough, itself, to produce equilibrium stripping of the projectile and the reaction products.

## III. THE DATA

In this section we will present the raw experimental data and the procedures used to extract differential and total cross sections for the orbiting yields. In the process, sources of experimental difficulty and uncertainty will be addressed.

The target used was a mixture of nitrogen and xenon in a 200:1 relative atomic abundance. Its thickness was determined through detection of elastically scattered particles from a $^{28}Si$ ion beam. The smallest available entrance aperture on the spectrograph ($\Delta\Omega=0.075$ msr) was used in this measurement. Figure 5 shows the yields of such $^{28}Si$ ions plotted as functions of position along the front wire of the HIC. Four atomic charge states of $^{28}Si$, identified to be $q=10^+$, $11^+$, $12^+$, and $13^+$, are shown. The two peaks for each of the charge states correspond to scattering from the $N_2$ and the Xe target nuclei, respectively. The lack of resolution of the $10^+$ yield is a consequence of edge effects. such spectra were measured at 130, 140, and 160 MeV $^{28}Si$ laboratory bombarding energies. By summing over the charge state yields in the peaks corresponding to the two target components, under the assumption of Rutherford scattering, the target thickness was determined to be $2.81\times10^{17}$ atoms/cm$^2$ for $N_2$ and $1.38\times10^{15}$ atoms/cm$^2$ for Xe.

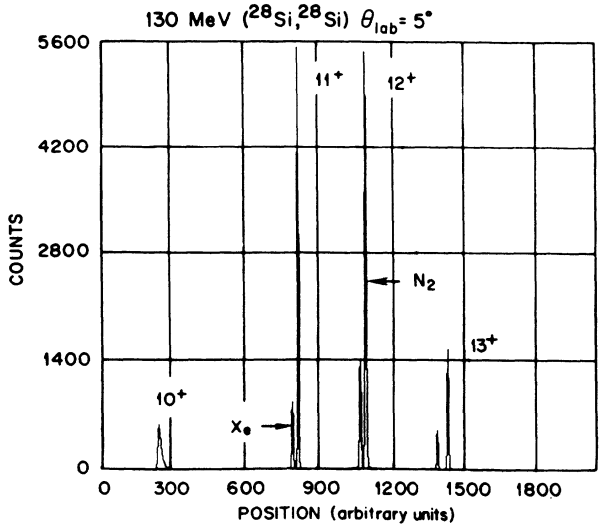


FIG. 5. Spectrum of elastically scattered $^{28}Si+^{14}N$ interaction. The channel numbers of the maxima are used in conjunction with information on the Enge magnet optics in order to obtain a calibration, in mm, of the position sensing wires.

The measured relative abundance of the two atomic species was 204:1. The beam current information was obtained, as noted previously, by integrating the charge delivered to the body of the gas jet apparatus. The absolute error in these measurements was less than 10%, including contributions from both the variance of detector efficiency with position along the front wire, and any error introduced by inexact beam current integration. The variance of detector efficiency we attribute to an insufficient width, in the vertical direction, of the HIC absorber window for trajectories with their focus far removed from the location of the position sensing wire. The target is free from contaminants and its thickness has been shown not to vary with time.

In this experiment we focus upon the targetlike reaction products emitted into forward angles; hence, the detection of beamlike particles, which are much more abundant, serves only to saturate the data acquisition system. Also, since the target thickness was known and the beam current integration procedure found to be reliable, it was no longer necessary to monitor the elastic events for normalization purposes. We therefore introduced a combination of gas and solid absorbers in front of the HIC to prevent the scattered $^{28}Si$ from entering the detector. Figure 6 shows spectra of orbiting products detected on the front and rear position wires; not all particles that pass the front wire manage likewise past the second. It bears emphasis that the segmented $\Delta E$ anode lies between the position sensing wires (see Fig. 3); hence, not all particles that produce a $\Delta E$ signal, produce a $W2$ signal. This will be demonstrated below.

Figure 7 shows the yields of orbiting products plotted as functions of their energy and energy loss as detected in the HIC. A low-pressure foldover is indicated for the raw $\Delta E1$ carbon yield in 7(a). This arises because the pressure of the gas in the HIC is not sufficient to stop, within the counter, the carbon ions with the highest energies. Spectra (a) and (b) have substantial backgrounds arising from counter edge effects. By the introduction of

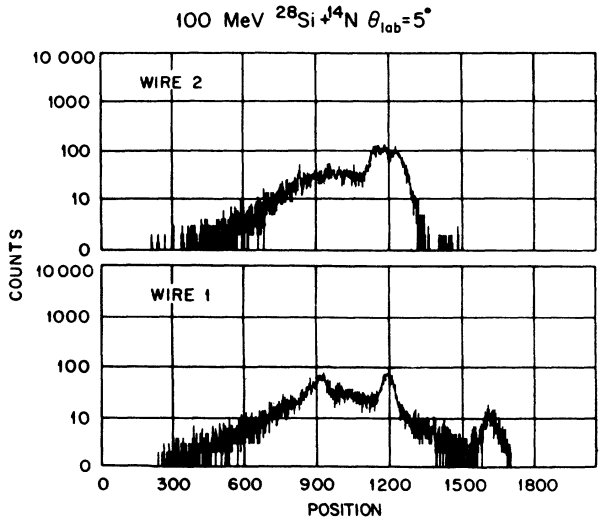


FIG. 6. Spectra of orbiting yields detected on the front and rear position sensing wires in the HIC.

a software gate between wire channels 450 and 1450, the spectra are improved significantly, as shown in panels (c) and (d).

We used software gates to distinguish between the various atomic species to obtain spectra such as those shown in Fig. 8. This figure shows the nitrogen yield plotted as functions of energy, and position along the front wire. There are two groups of three lines corresponding to the nitrogen being detected with the atomic charge states $7+$ and $6+$. The yield is concentrated in the higher charge state, as expected, because of the presence of a stripper foil at the entrance to the spectrograph. The dynamic range of particles detected in the HIC is limited by two factors: namely, the dispersion of the magnet, and the pressure in the HIC. The first factor arises because of the finite width of the HIC; below channel 90, and above channel 400 on the position axis in Fig. 8, there are no counts because these represent the limits of the software gate imposed to eliminate counter edge effects. This manifests itself as a low-energy cutoff for the $7+$ charge state yield. For the $6+$ yield, however, this results in a high energy cutoff. This is one reason why, at each energy, we have to collect data at different magnetic field settings in order to detect optimally the different atomic species. Before discussing pressure cutoffs, we should point out that the position spectra are defocused at the high energy end of the $7+$ yield and focused at the low energy end. This has to do with the relative position of the focal plane of the spectrograph and the plane of the position sensing wire. These two planes intersect close to channel 400, and are at an angle of about 45° to each other.

The reaction products go through several layers of energy absorbing material before entering the HIC. Some products, such as the elastic yield, are stopped before they enter the HIC. This also happens to the yields of some of the lower energy products of orbiting reactions. Even if these reaction products do manage to enter the counter, not all of them deposit enough energy in the HIC to permit unambiguous identification of their charge and mass. They are lost in the low energy foldover of the $E$ versus $\Delta E$ spectrum (Fig. 7). If, however, the pressure of gas in the HIC is not sufficient to stop the particles within the counter, we observe a high energy foldover as shown in Fig. 9. The individual lines corresponding to the different isotopes of the same element overlap, making a separation of their yields ambiguous. This foldover also affects the energy signal; we can, however, extract energy information from the position signal. This can be accomplished by using magnet calibration information.

Shown in Fig. 10 are the projections along the energy and position axes of the $7^+$ $^{14}$N yield of Fig. 8. Discrete maxima are observed in the energy spectrum that are washed out in the position spectrum because of the effects of focusing in the spectrograph. We can, in principle, use the position information from wires $W1$ and $W2$ to calculate what the position spectrum should look like on the focal plane. Figure 11 shows the position spectra of the nitrogen yields of Fig. 9 (The vertical scale here is now logarithmic). Also shown are spectra calcu-

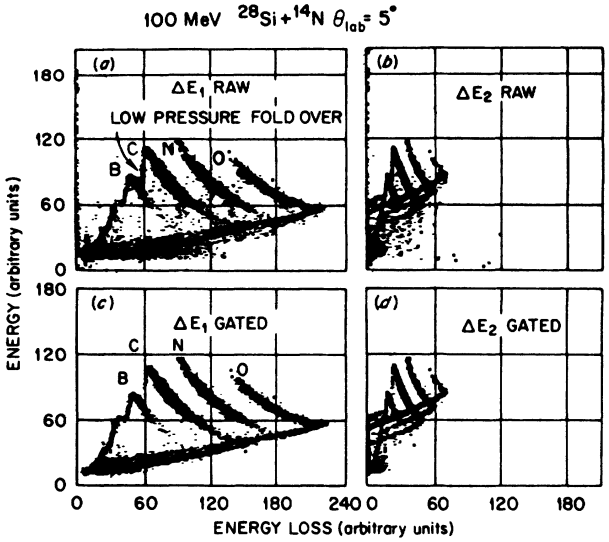


FIG. 7. Spectra of orbiting yields plotted as functions of energy and energy loss as detected in the HIC.

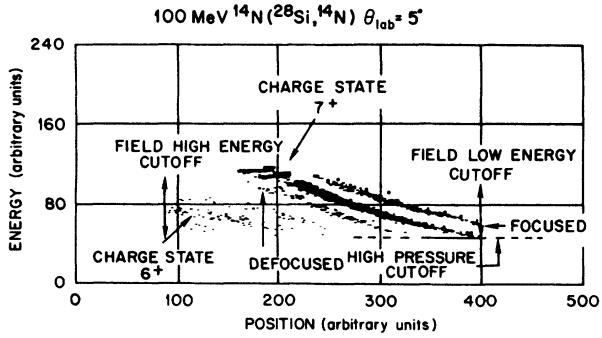


FIG. 8. The $Z$-gated energy vs wire position spectrum of orbiting products for the nitrogen channel in the $^{28}$Si+$^{14}$N reaction. The position axis in this figure plots distance, in millimeters, along the front wire, from an unspecified origin. The position information is obtained from a calibration using the position channel information from Fig. 8.

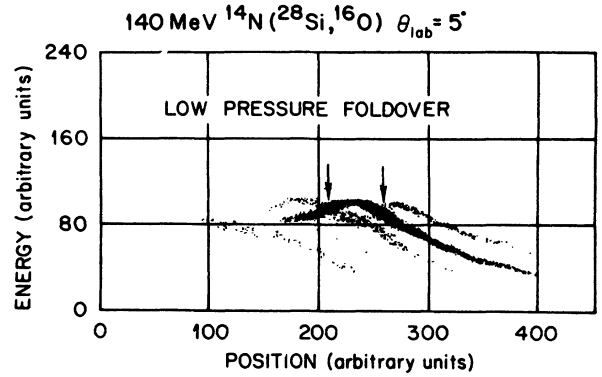


FIG. 9. Spectrum of oxygen yields from a $^{28}$Si+$^{14}$N interaction plotted as functions of energy and wire position. The figure shows the effects of a high energy foldover, because the HIC does not have enough gas pressure to stop the oxygen ions within the detector.

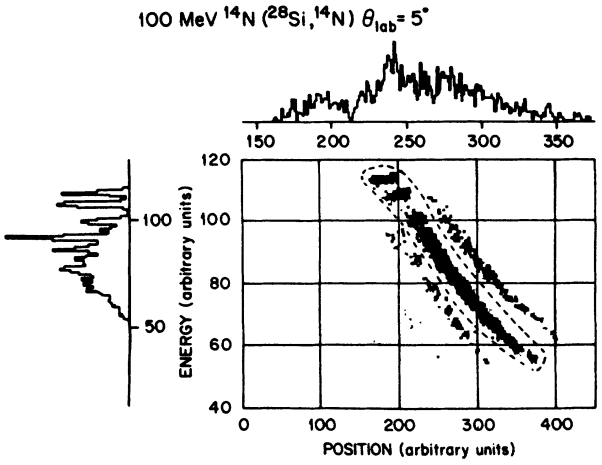


FIG. 10. Projection along the energy and position axes of the $^{14}N$ yield within the gate.

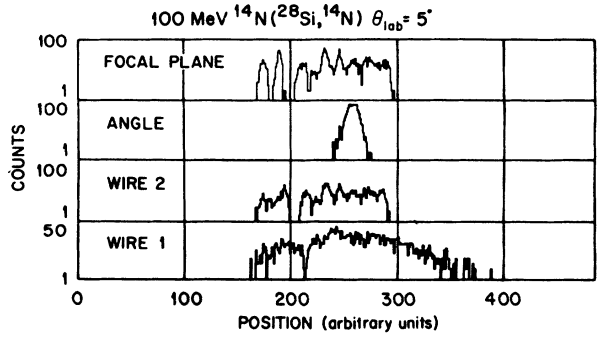


FIG. 11. $^{14}N$ yields plotted as functions of wire 1 position, wire 2 position, opening angle subtended by ion trajectories, and position on a focal plane. The focal plane and angle spectra are calculated by "ray tracing."

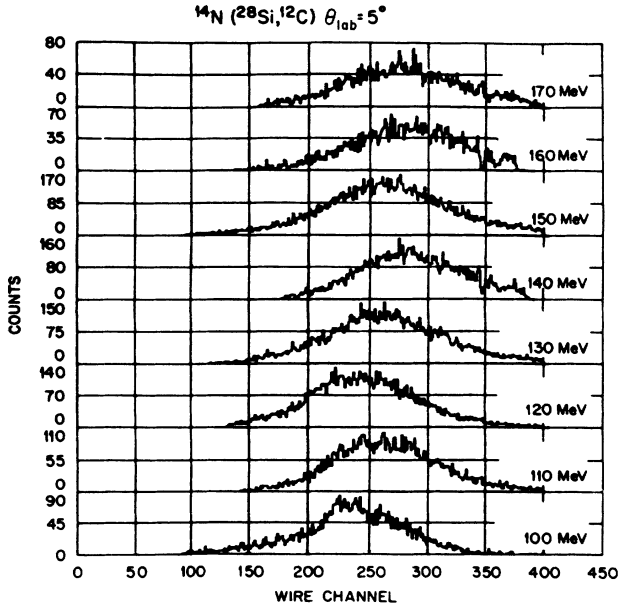


FIG. 12. The yield of $^{12}C$ nuclei from the $^{28}Si+^{14}N$ interaction plotted as functions of the position along the front wire in the HIC. The data shown are for $^{28}Si$ laboratory bombarding energies between 100 and 170 MeV.

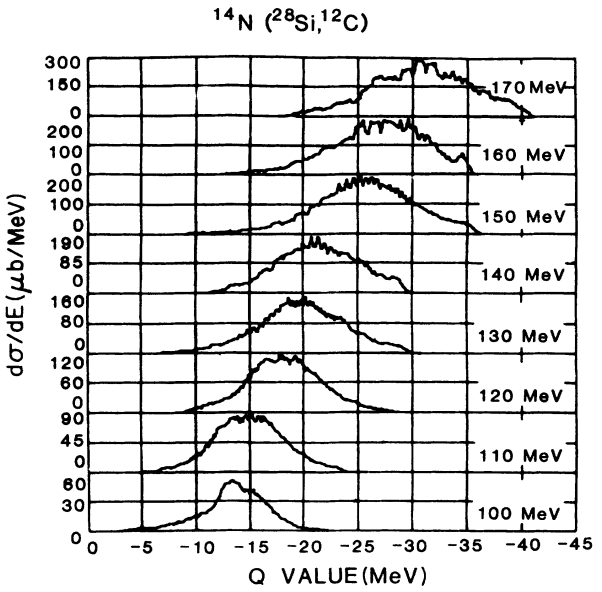


FIG. 13. The orbiting cross sections of $^{12}C$ nuclei from the $^{28}Si+^{14}N$ interaction plotted as functions of $Q$ value. The data shown are for $^{28}Si$ laboratory bombarding energies between 100 and 170 MeV.

lated for the yields projected onto the focal plane and the angles of incidence of the ion trajectories on the focal plane. These are obtained by ray tracing. In this procedure, the position information from the two wires, for a particular trajectory, is used to see where such a trajectory intersects the focal plane. It is clear that such a procedure produces position spectra that show maxima just like the energy spectrum of Fig. 10. It is also clear from Fig. 11 that it is for only those trajectories that have both front and rear wire signals that the ray tracing procedure is applicable. It is for this reason that we cannot use the focal plane spectra to determine cross sections and kinetic energies of reaction products. It is possible, however, to use the information provided by the front wire for this purpose.

Figure 12 shows projections onto the position axis from spectra similar to Fig. 10, at several laboratory bombarding energies, for the $^{12}C$ channel. The total counts in such spectra were then normalized by the total current integrated during the corresponding measurements, in order to obtain differential cross sections.

Figure 13 shows the angle-integrated absolute orbiting cross sections for $^{12}C$ nuclei plotted as functions of $Q$ value. These spectra were obtained from those shown, for example, in Fig. 12, using a rebinning procedure. The oscillations in the spectra are an artifact of this procedure. It can be shown, through a study of the mean values of such spectra, that we are observing the effects of angular momentum limitation on the formation of the $^{28}Si+^{14}N$ dinuclear molecule as had been observed in the $^{28}Si+^{12}C$ case. Equivalent spectra for the $^{14}N$ and $^{11}C$ exit channels are shown in Ref. 6.

The excitation energy and angle-integrated, absolute, orbiting cross sections can then be extracted from such data, as functions of center of mass bombarding energy.

In obtaining these cross sections, the $1/\sin\theta$ behavior observed at backward angles for the differential cross sections were assumed to persist into the forward angles, and accordingly accounted for.

### A. A note on experimental uncertainties

The orbiting cross sections for the various exit channels are tabulated in Table I. The statistical uncertainty in the cross section determination for the three strongest channels $^{12}C$, $^{14}N$, and $^{16}O$ is of the order of 2%. For the other carbon, nitrogen, and oxygen channels the corresponding number is about 7% and for the boron, fluorine, and neon channels about 12%. There are two primary sources of systematic error in these measurements. The HIC detection efficiency varies with position along the front wire as determined through a study of the elastic yield of $^{28}Si$ from the $^{28}Si+^{14}N$ interaction. This uncertainty is less than 10% and includes contributions from the current integration procedure. For alpha particles, however, this efficiency has been measured to be fairly constant, with a statistical uncertainty of around 2%, and negligible systematic uncertainty. For reaction products of intermediate mass, we can assume that, because of an intermediate kinematic shift, these are of intermediate size (about 5%). Uncertainties are also introduced by the pressure and field limitations discussed in Figs. 8 and 9. These are minimized for the exit channel for which the magnetic field and detector pressure have been optimized. In particular, they are small for the $^{12}C$ and $^{16}O$ exit channels and slightly larger for the $^{14}N$. The information for the $^{14}N$ channel was obtained mostly from settings optimized for the $^{12}C$ and $^{16}O$ channels, respectively. From the shape of the $^{14}N$ spectra, one can estimate the magnitude of these errors to be less than 10% for both cross section and average kinetic energy determinations.

The total uncertainty on the experimental quantities obtained by adding these various contributions in quadrature is $\approx 11\%$ for the three strongest channels. Comparisons between several independent measurements of the kinetic energies and cross sections for these channels show mutual agreement at around the 10% level. For the other nitrogen, carbon, and oxygen channels, these uncertainties are larger, and lie in the range 15–20%. For the weakest channels, equivalent numbers are difficult to estimate, owing to severe cutoffs in the spec-

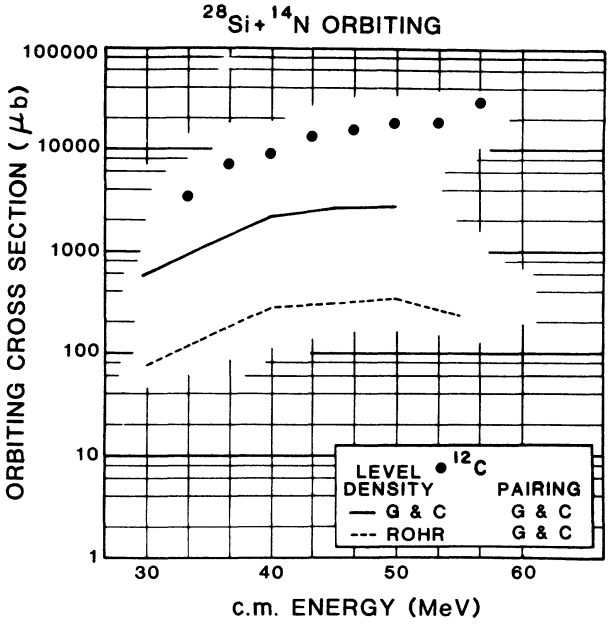


FIG. 14. $^{12}C$ orbiting yields from the $^{28}Si+^{14}N$ interaction. The data are shown as solid circles. The curves are the results of compound nucleus-type calculations (Ref. 11). Solid line denotes Gilbert Cameron level density and pairing (Ref. 12). Dashed line denotes Rohr level density (Ref. 13), and Gilbert-Cameron pairing (Ref. 12).

TABLE I. Orbiting cross sections for several exit channels from the $^{28}Si+^{14}N$ interaction. The uncertainties on these numbers are discussed in the text.

| Channel \ $E_{c.m.}$ / $E_{lab}$ | 33.3 / 100 | 36.7 / 110 | 40 / 120 | 43.4 / 130 | 46.7 / 140 | 50.0 / 150 | 53.3 / 160 | 56.7 / 170 |
|---|---|---|---|---|---|---|---|---|
| $^{10}B$ | 0.23 | 0.63 | 0.91 | 1.37 | 2.0 | 2.72 | 3.0 | 4.0 |
| $^{11}B$ | 0.05 | 0.132 | 0.17 | 0.28 | 0.56 | 0.67 | 1.0 | 2.00 |
| $^{11}C$ | 0.078 | 0.174 | 0.349 | 0.374 | 0.44 | 0.910 | 1.2 | 2.44 |
| $^{12}C$ | 3.2 | 7.0 | 9.46 | 13.03 | 15.16 | 19.7 | 19.3 | 29.63 |
| $^{13}C$ | 0.22 | 0.5 | 0.6 | 1.0 | 1.93 | 2.1 | 2.75 | 5.23 |
| $^{13}N$ | 0.148 | 0.244 | 0.348 | 0.380 | 0.393 | 0.65 | 0.85 | 0.87 |
| $^{14}N$ | 1.06 | 1.93 | 2.33 | 2.86 | 3.39 | 4.7 | 5.5 | 8.08 |
| $^{15}N$ | 0.06 | 0.15 | 0.24 | 0.41 | 0.64 | 0.93 | 1.3 | 2.56 |
| $^{15}O$ | 0.093 | 0.222 | 0.38 | 0.54 | 0.62 | 1.06 | 1.01 | 1.75 |
| $^{16}O$ | 0.92 | 1.91 | 3.58 | 5.28 | 6.23 | 8.07 | 8.99 | 12.83 |
| $^{17}O$ | 0.04 | 0.117 | 0.3 | 0.56 | 0.888 | 1.1 | 1.33 | 1.86 |
| $^{17}F$ | 0.001 | 0.003 | 0.007 | 0.012 | 0.019 | 0.024 | 0.028 | 0.04 |
| $^{18}F$ | 0.21 | 0.5 | 0.88 | 1.17 | 1.52 | 1.61 | 1.81 | 2.6 |
| $^{19}F$ | 0.005 | 0.02 | 0.06 | 0.12 | 0.18 | 0.26 | 0.34 | 0.59 |
| $^{19}Ne$ | 0.0 | 0.0 | 0.04 | 0.02 | 0.12 | 0.13 | 0.05 | 0.11 |
| $^{20}Ne$ | 0.0 | 0.0 | 0.43 | 0.43 | 1.13 | 1.12 | 0.538 | 0.94 |
| $^{21}Ne$ | 0.0 | 0.0 | 0.04 | 0.1 | 0.43 | 0.39 | 0.17 | 0.37 |

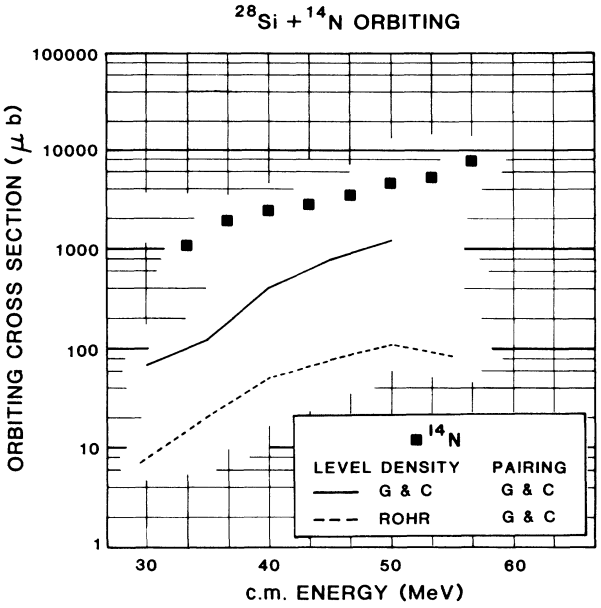


FIG. 15. $^{14}N$ orbiting yields from the $^{28}Si+^{14}N$ interaction. The data are shown as solid squares. The curves are the results of compound nucleus-type calculations (Ref. 11). Legends same as Fig. 14.

tra. These quoted cross sections should, therefore, be treated with caution and as lower estimates of the real values.

Figures 14–16 show the orbiting cross sections for the three strongest channels $^{14}N$, $^{12}C$, and $^{16}O$ plotted as functions of the center of mass energy. The data are shown as points, and the lines are predictions of a compound nucleus evaporation calculation,[11] to be discussed below. From these data it is obvious that at nearly all energies the $^{12}C$ and $^{16}O$ yields exceed those of $^{14}N$. One can therefore conclude that the duration of orbiting in this interaction is sufficiently long to permit the equilibration of charge and mass. This follows, since the yields in the $^{12}C$ and $^{16}O$ exit channels are larger than that in the $^{14}N$ exit channel, which is the entrance channel for this measurement. The exit channel yields seem therefore to be determined by phase space considerations.[6,7]

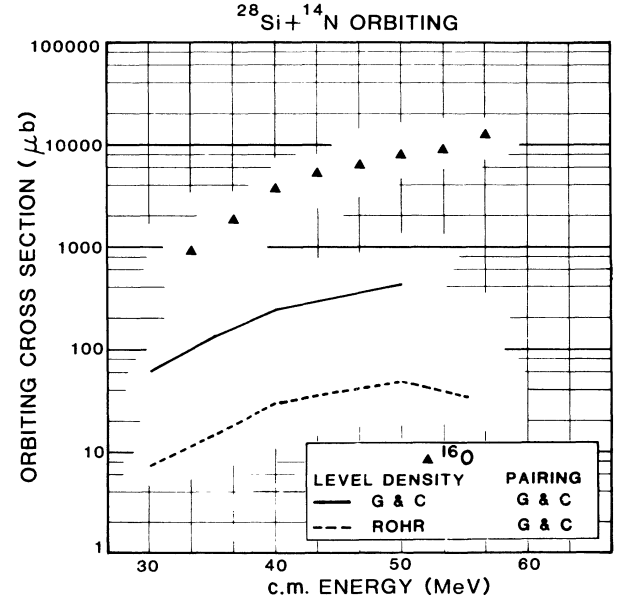


FIG. 16. $^{16}O$ orbiting yields from the $^{28}Si+^{14}N$ interaction. The data are shown as solid triangles. The curves are the result of compound nucleus-type calculations (Ref. 11). Legends same as Fig. 14.

## IV. DISCUSSION

We noted above that a composite system is formed in the early stages of the interaction between $^{28}Si$ and $^{14}N$ nuclei. This composite, we have maintained, has a dinuclear shape and is not the compound nucleus. One of the reasons for making this distinction follows from the fact that traditional Hauser-Feshbach compound nucleus evaporation calculations have failed to reproduce the magnitudes of the cross sections for the emission of fragments with masses near that of the target or heavier. Shown in Figs. 14–16 are the results of two such calculations.[11] The upper curve uses values for the level density factor $a$ and pairing corrections as tabulated in Ref. 11, whereas the lower curve uses the same pairing energies but uses the factors $a$ as given in Ref. 12. The calculated yield is that of nuclei that are expected to survive particle decay subsequent to being produced in an excited state in the interaction. It is clear that while the first calculation is more successful in reproducing the trend of the observed cross sections, the two calculations still underpredict the orbiting yields by one to two orders of magnitude.

Figures 17–19 show the same data together with predictions of an orbiting model.[14,15] The value of the level density constant $a$ for these calculations is taken to be

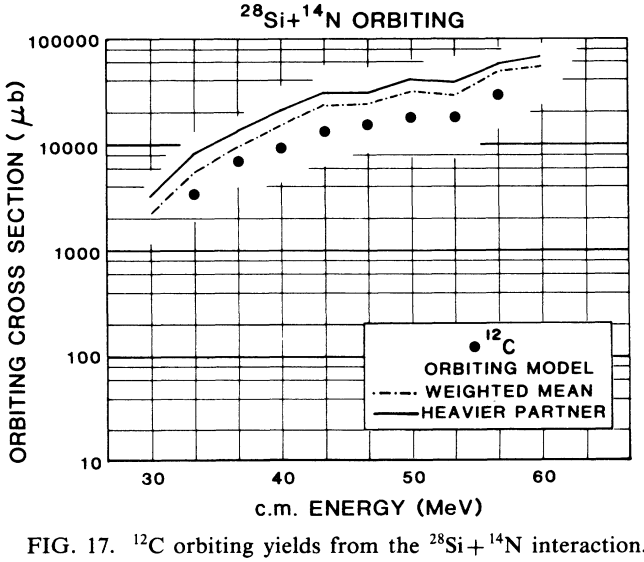


FIG. 17. $^{12}C$ orbiting yields from the $^{28}Si+^{14}N$ interaction. The data are shown as solid circles. The curves are the results of orbiting-type calculations (Refs. 14 and 15). Solid line denotes pairing energy of heavier partner. Dashed line denotes mass weighted mean of pairing energies.

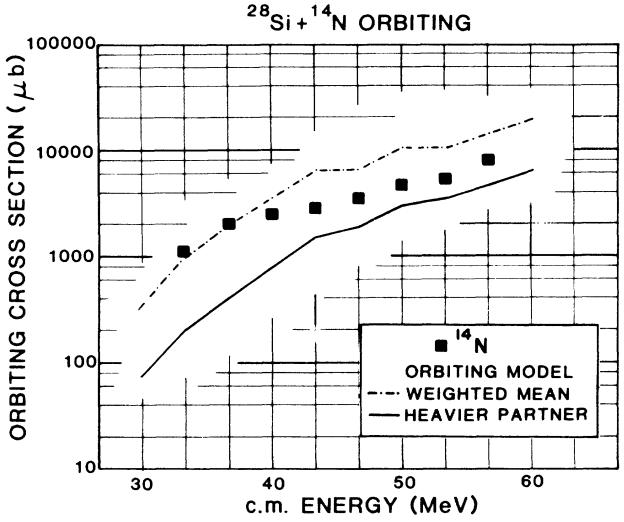


FIG. 18. $^{14}N$ orbiting yields from the $^{28}Si+^{14}N$ interaction. The data are shown as solid squares. The curves are the results of orbiting-type calculations (Refs. 14 and 15). Legends same as Fig. 17.

5.25. The two curves shown for each exit channel correspond to two prescriptions used in the calculation of the pairing energy. For each exit channel, the dashed curve uses the weighted mean of the pairing energies of the two nuclei constituting the composite system; the solid curve uses the pairing energy of the heavier partner in the composite. The results of these calculations are clearly more successful in reproducing the data than are the compound nucleus ones. It is worth pointing out that the prescription used in the calculation of the pairing energies for the solid curve reproduces the correct ordering for the magnitudes of the observed yields: $^{12}C > ^{16}O > ^{14}N$. Such an ordering cannot be reproduced by standard compound nucleus calculations. It is also worth recalling that the calculated orbiting yields are

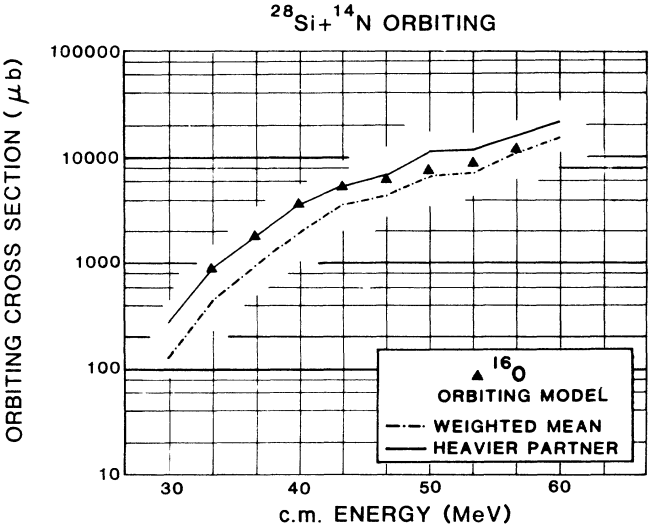


FIG. 19. $^{16}O$ orbiting yields from the $^{28}Si+^{14}N$ interaction. The data are shown as solid triangles. The curves are the results of orbiting-type calculations (Refs. 14 and 15). Legends same as Fig. 17.

determined by the way the available phase space for the outward decay of the composite nuclear system is parametrized. The solid curve predicts higher yields for the $^{12}C+^{30}P$ and $^{16}O+^{26}Al$ channels than does the dashed curve, whereas lower yields are predicted for the $^{14}N+^{28}Si$ channel. What bears emphasis here is the "odd-odd" nature of the heavier partner in the case of the first two channels, and its even-even nature in the third. In the context of the orbiting calculations, the data seem to favor a prescription for the pairing energy intermediate between those chosen. Further measurements on the details of energy division between the products from orbiting interactions are needed in order to address these questions quantitatively. In performing these calculations, one has to keep in mind that the fusion cross section associated with the $^{28}Si+^{14}N$ interaction is expected to peak around 1000 mb. This number is predicted by the orbiting calculations and is used as an input to the compound nucleus evaporation calculations. The compound nucleus model describes the emission of particles from an equilibrated compound nucleus via thermal evaporation. The emission of massive fragments, in such a scenario, is a rather improbable event. In the orbiting model, however, the emission of massive fragments results from the breakup of a dinuclear composite, and this happens prior to the formation of a compound nucleus, and with higher probability.

We suggest that the distribution of product yields among the open exit channels is governed by phase space considerations. To this end it is useful to examine the widths of the mass distributions for the three dominant exit channels. This is a concise way of describing how the mass yield is distributed over the various exit channels, including those for which $N$ is not equal to $Z$. Figure 20 is a plot of these mass witdths for the carbon, nitrogen, and oxygen exit channels. They are the widths of Gaussians obtained by fitting three points determined by the isotopic yields in the three mass groups associated with each element (see Figs. 8–10 and Table I). The curves are predictions of the orbiting model[14,15] obtained using the same prescriptions as for Figs. 17–19. The widths for the carbon channel appear to be constant at a value of 0.4 up to a center of mass energy of 45 MeV. Above this energy, they show a smooth increase in value. The break in these data appears to be correlated with a corresponding break in the kinetic energy of orbiting products for the same exit channel (discussed in reference to Fig. 21). The data shown in Fig. 20 for the nitrogen and oxygen channels, on the other hand, do not show such behavior. The data demonstrate that there is substantial orbiting yield in channels other than those for which $N=Z$. While the model is able to reproduce some trends seen in the data, the mass widths for the carbon and oxygen channels are systematically underpredicted. The model predictions for the $^{14}N$ channel (where the heavier partner is an even-even nucleus) depend significantly on the choice of the pairing prescription, as was the case for the predictions of the orbiting cross sections (Figs. 17–19).

Figure 21 shows the final kinetic energies of the carbon, nitrogen, and oxygen nuclei, emitted from orbiting

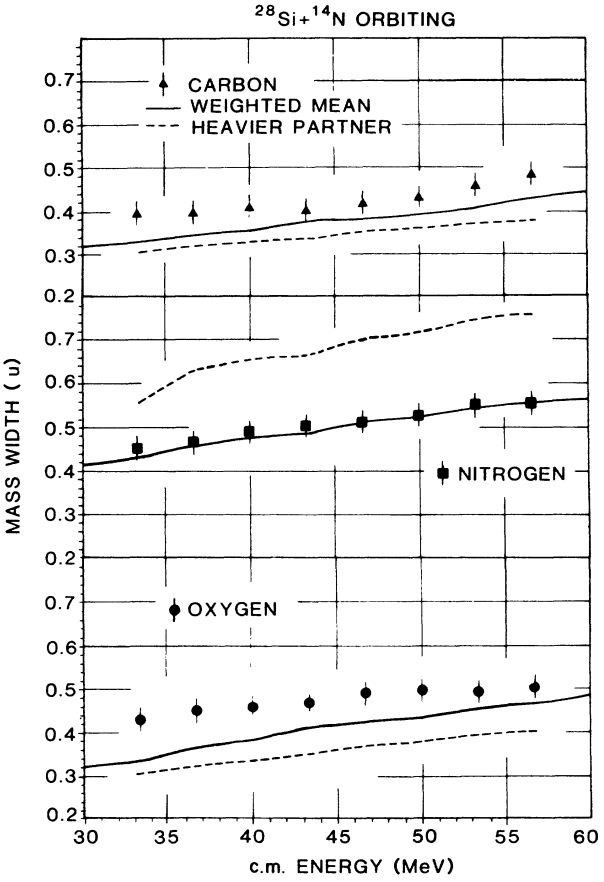


FIG. 20. Mass widths of orbiting yields of the carbon, nitrogen, and oxygen exit channels in the $^{28}Si+^{14}N$ orbiting interaction. The curves are predictions of the orbiting model (Refs. 14 and 15). Solid line denotes mass weighted mean of pairing energies. Dashed line denotes pairing energy of heavier partner.

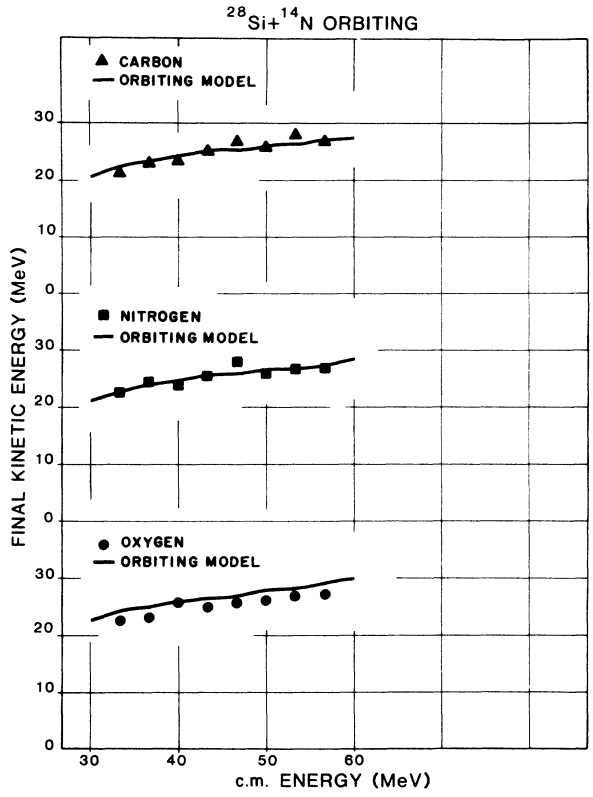


FIG. 21. The final kinetic energies of orbiting products from the $^{28}Si+^{14}N$ interaction plotted as functions of center of mass energy. The solid lines are predictions of the orbiting model (Refs. 14 and 15).

interactions, plotted as functions of center of mass energy. The final kinetic energies correspond to the potential energy stored in an orbiting dinuclear system just prior to scission. In terms of a nucleus-nucleus potential for such light heavy-ion composites, this represents, approximately, the top of the outer maximum for the highest partial wave contributing to the orbiting process. Since orbiting composites are formed only for those partial waves for which the nucleus-nucleus potential exhibits a local minimum, there is a limit to the angular momentum that the orbiting composite can sustain. This is reflected in the kinetic energy data by a saturation in the product final kinetic energies as was seen for the $^{28}Si+^{12}C$ system.[2] There appears to be some evidence for such behavior in the data for the three exit channels, and more strongly so for the carbon and nitrogen channels than for the oxygen. The data, however, are not as definitive as are those for the $^{28}Si+^{12}C$ system; this probably reflects the fact that there are more open exit channels in the $^{28}Si+^{14}N$ than in the $^{28}Si+^{12}C$ system. As noted previously, the change in the slope of the kinetic energy data occurs at a c.m. energy of 45 MeV, correlated with the change in shape of the carbon mass width (Fig. 20). The reason for this is that for a fixed partial wave, the more the available excitation energy, the larger the number of open exit channels and the greater the mass width. At a c.m. energy less than 45 MeV, the excitation energy does not increase as rapidly as the center of mass energy because an increasing number of partial waves contribute to the orbiting process. The mass width, therefore, remains unchanged. When the angular momentum saturates, increases in the center of mass energy result directly in increases in the excitation energy. Hence, more exit channels open and the mass width increases. While this feature appears in the data for the dominant exit channel ($^{12}C$), it is not distinct in the data for the weaker channels, particularly in case of the mass width data. It is worth noting that the mean of the mass distribution does not change appreciably, as would have been the case if the increase in mass width had come about as a result of secondary emission (see Table I). The curves in Fig. 21 are the predictions of the orbiting calculation for the exit channel fragment kinetic energies. The predictions of the model under the two prescriptions discussed above are indistinguishable, and the model is able to provide a quantitative reproduction of the data. In the context of the orbiting model, the saturation of the exit channel kinetic energies translates to a saturation of the angular momentum in the $^{28}Si+^{14}N$ orbiting dinuclear system at

$l_{cr}=26\hbar$. This implies that incoming partial waves with $l>26\hbar$ cannot become trapped, and therefore, do not contribute to either the orbiting process or to fusion.[14]

Figure 22 shows the charge widths of yields from the $^{28}Si+^{14}N$ orbiting interaction plotted as functions of the center of mass energy. The widths shown here are those of inverted Gaussians fitted through three points represented by the yields in the dominant channels $^{12}C$, $^{14}N$, and $^{16}O$. The uncertainties of the data (solid circles) are the uncertainties derived from the experimental cross sections. As in previous figures, the curves are the predictions of the orbiting model. The data indicate that the charge width decreases up to a center of mass energy of $\approx 45$ MeV and then begins a gradual increase. The decrease at lower energies is a reflection of the fact that the cross sections for the carbon and oxygen channels are increasing much faster than that for the nitrogen channel. At higher energies this trend is partially reversed because of the increasing number of other exit channels available to the orbiting system. The theoretical predictions share the trend shown by the data at the higher energies but fail to reproduce the low energy behavior. This may be attributable to incomplete charge and mass equilibration in the $^{28}Si+^{14}N$ interaction at low excitation energies. Since the model assumes full equilibration, it also predicts a much steeper dropoff in the $^{14}N$ exit channel yield at low energies than is observed in the data (Fig. 18). As discussed previously,[6] energy can be dissipated in orbiting interactions through both inelastic excitation and particle exchange. The $^{12}C$ and $^{16}O$ exit channels can be populated from the $^{14}N$ entrance channel through the sequential exchange of a proton and a neutron. At low excitation energies, the single nucleon transfer channels are not easily accessible, and the equilibration of charge and mass through single particle exchange is hindered. The equilibrium model is therefore unable to reproduce the yield in the $^{14}N$ entrance channel. At higher excitation energies, the single particle transfer modes become accessible, and phase space equilibrium is established. This change in behavior from incomplete to complete equilibration, from a phase space perspective, occurs at a center of mass energy of $\approx 45$ MeV and correlates with the energy at which the final fragment kinetic energy saturates (Fig. 21) and also the energy at which the mass width in the carbon channel (Fig. 20) begins to increase. It seems reasonable to conclude from this that descriptions of the orbiting process must include in their formulation some information on how equilibrium is approached, in addition to the information concerning the phase space accessible after equilibration has occurred. Also, as stated previously, the sum total of the data seem to favor the use of a pairing prescription, in the orbiting model, intermediate between these chosen above.

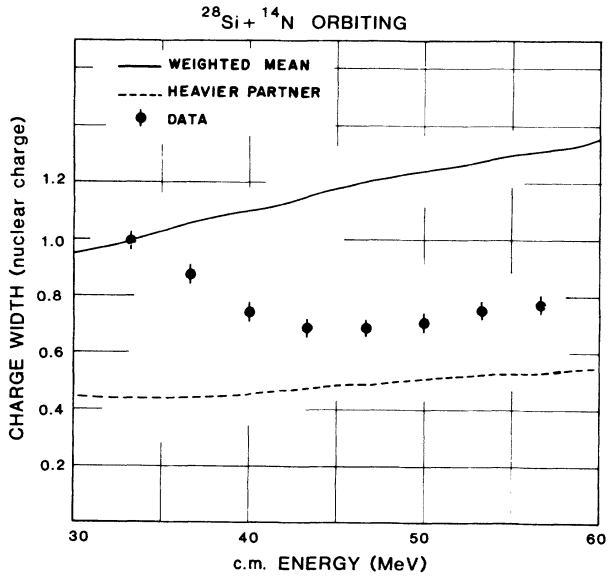


FIG. 22. Charge widths of orbiting yields in the three dominant exit channels—carbon, nitrogen, and oxygen—plotted as functions of center of mass energy. The curves are the predictions of the orbiting model (Refs. 14 and 15). Legends same as Fig. 20.

The absolute magnitude of the orbiting cross section summed over the various exit channels amounts, at the highest energies, to about 70 mb. This number is smaller than the equivalent number for the $^{28}Si+^{12}C$ interaction.[2] A possible explanation for this may lie in the way the yield in the highest partial waves are divided between the orbiting and nucleon transfer processes (which would occur with greatest probability near the grazing angle). It would, therefore, be of interest to compare the nature of the transfer cross sections in the $^{28}Si+^{14}N$ and $^{28}Si+^{12}C$ interactions.

A detailed study of orbiting interactions in the low energy region ($E_{c.m.}<45$ MeV) may shed further light on the details of particle transfer and energy dissipation in heavy ion reactions and in the $^{28}Si+^{14}N$ interaction in particular. A complementary study has already been suggested in investigating the $^{16}O+^{24}Mg$ interaction.[7] Studies of orbiting in other entrance channels populating the same composite system could be used to determine the critical angular momentum $l_{cr}$ as has been done in the case of fusion reactions. Such a study could shed light on how the orbiting process influences the strong dependence observed, in studies of fusion cross sections, of $l_{cr}$ on mass asymmetry.[16] In particular, it would be of interest to study the process of fusion in $^{28}Si+^{14}N$ interactions to see if the $l_{cr}$ extracted from the fusion data agrees with that extracted from the orbiting data.

Measurements of the alignment of the reaction products from orbiting interactions in $^{24}Mg+^{12}C$ (Ref. 17) and $^{28}Si+^{12}C$ (Ref. 18) have indicated alignments in excess of 90%. This needs investigation for DMC's with both zero and nonzero entrance channel spin, and would provide a way to investigate possible dealignments that nonzero entrance channel spins (as in the $^{28}Si+^{14}N$ interaction) may experience. It would also be of interest to measure the alignment in channels other than the entrance channel to shed further light on the nature of orbiting reactions.

Studies of the duration of the orbiting process in the $^{24}Mg+^{12}C$ system[5] have indicated orbiting lifetimes of the order of $2\times 10^{-21}$ s. It would be interesting to make

similar measurements in the $^{28}Si+^{14}N$ system to see whether there is a correlation between the number of particles exchanged and the orbiting lifetime.

## V. SUMMARY AND CONCLUSIONS

We have studied the charge and mass distribution of orbiting yields from the $^{28}Si+^{14}N$ interaction. The data indicate that the orbiting system lives sufficiently long for the exit channel yields to be determined by the accessible phase space. We have compared the data with compound nucleus and orbiting calculations and have found that the data clearly favor the latter. Further comparisons between the data and the orbiting calculations indicate that full phase space equilibration of the orbiting yields is hindered at low excitation energies by the inaccessibility of single nucleon transfer channels. Also evident in the data is a correlation in the behaviors of the charge width, mass width, and final product kinetic energies of orbiting yields, and these are interpretable as arising from saturation in the angular momentum that the $^{28}Si+^{14}N$ orbiting composite can sustain. Several questions arise as a result of this study and we have indicated in the text avenues for future investigation, both experimental and theoretical.

## ACKNOWLEDGMENTS

This work was supported in part by Contract No. DE-AC02-76ER0374 with the U.S. Department of Energy (U.S. DOE). Oak Ridge National Laboratory is operated by Martin Marietta Energy Systems, Inc., under Contract No. DE-AC0584OR21400 with the U.S. DOE.

---

*Present address: Lawrence Berkeley Laboratory, Berkeley, CA 94720.

[1]R. Eggers, M. N. Namboodiri, P. Gonthier, K. Georffroy, and J. B. Natowicz, Phys. Rev. Lett. **37**, 324 (1976).

[2]D. Shapira, D. Schull, J. L. C. Ford, Jr., B. Shivakumar, R. L. Parks, R. A. Cecil, and S. T. Thornton, Phys. Rev. Lett. **53**, 1634 (1984).

[3]I. Iori, M. Gentilli, I. Massa, F. Vannini, P. Baccaccio, F. Reffo, L. Vanucci, and R. A. Ricci, Phys. Lett. **132B**, 304 (1983).

[4]A. Ray, S. Gil, M. Khandaker, D. D. Leach, D. K. Lock, and R. Vanderbosch, Phys. Rev. C **31**, 1573 (1985).

[5]A. Glaesner, W. Dunnweber, W. Hering, D. Konnerth, R. Ritzka, R. Singh, and W. Trombik, Phys. Lett. **169B**, 153 (1986).

[6]B. Shivakumar, D. Shapira, P. H. Stelson, B. A. Harmon, K. Teh, M. Beckermann, and D. A. Bromley, Phys. Rev. Lett. **57**, 1211 (1986).

[7]B. Shivakumar, Ph.D. thesis, Yale University, 1986.

[8]D. Shapira, R. Novotny, Y.-D. Chan, K. A. Erb, J. L. C. Ford, Jr., J. C. Peng, and J. D. Moses, Phys. Lett. **114B**, 111 (1982).

[9]D. Shapira, J. L. C. Ford, Jr., R. Novotny, B. Shivakumar, R. L. Parks, and S. T. Thornton, Nucl. Instrum. Methods **228**, 259 (1985).

[10]D. Shapira, G. L. Bomar, J. L. C. Ford, Jr., J. Gomez del Campo, and L. C. Dennis, Nucl. Instrum. Methods **169**, 77 (1980).

[11]D. Shapira, B. Shivakumar, B. A. Harmon, and S. Ayik (unpublished).

[12]A. Gilbert and A. G. W. Cameron, Can. J. Phys. **43**, 1446 (1965).

[13]G. Rohr, Z. Phys. A **318**, 299 (1984).

[14]B. Shivakumar, S. Ayik, B. A. Harmon, D. Shapira, Phys. Rev. C **35**, 1730 (1987).

[15]S. Ayik, B. Shivakumar, and D. Shapira (unpublished).

[16]B. A. Harmon, D. Shapira, P. H. Stelson, B. L. Burks, K. A. Erb, B. Shivakumar, K. Teh, and S. T. Thornton (unpublished).

[17]W. Dunnweber, A. Glaesner, W. Hering, D. Konnerth, R. Ritzka, R. Singh, and W. Trombik, in Proceedings of the Second International Conference on Nucleus-Nucleus Collisions, Visby, Sweden, 1985, Vol. 1, p. 119 (unpublished).

[18]A. Ray, D. D. Leach, R. Vandenbosch, K. Lesko, and D. Shapira, Phys. Rev. Lett. **57**, 815 (1986).